Shell-model predictions for electromagnetic properties of $N=50$ nuclei

Xiangdong Ji
W. K. Kellogg Radiation Laboratory, California Institute of Technology, Pasadena, California 91125
and Department of Physics and Atmospheric Science, Drexel University, Philadelphia, Pennsylvania 19104

B. H. Wildenthal
Department of Physics and Astronomy, University of New Mexico, Albuquerque, New Mexico 87131
and Department of Physics and Atmospheric Science, Drexel University, Philadelphia, Pennsylvania 19104
(Received 9 August 1988)

Predictions for $E2$, $M1$, and $M4$ transition rates and moments, together with examples of transition-charge densities, are presented for states of $N=50$ nuclei. These predictions are based on one-body spectroscopic amplitudes obtained from the wave functions of a new $N=50$ shell-model calculation which incorporates the $0f_{5/2}$, $1p_{3/2}$, $1p_{1/2}$, and $0g_{9/2}$ single-particle orbits and an empirically determined effective Hamiltonian for this space. The predictions are compared with experimental data, first in order to evaluate how well the model space, as applied by this Hamiltonian, accounts for observations, and then to assess the importance of configurations excluded from the model space and to determine the values of the operator renormalizations (effective charges and effective g factors) which optimally map the theoretical results onto the corresponding experimental values.

I. INTRODUCTION

The $N=50$ isotones between ^{82}Ge and ^{96}Pd span two rather distinct regions of shell-model configurations. Above ^{90}Zr, the low-lying wave functions tend to be dominated by configurations constructed purely of $0g_{9/2}$ protons, or of $0g_{9/2}$ protons and $1p_{1/2}$ proton holes, while below ^{88}Sr the wave functions presumably are dominated by configurations constructed of mixtures of $0f_{5/2}$, $1p_{3/2}$, and $1p_{1/2}$ protons. We have attempted to unify these rather disparate regions of $N=50$ nuclei with a single model space, consisting of the $0f_{5/2}$, $1p_{3/2}$, $1p_{1/2}$, and $0g_{9/2}$ single-particle orbits, designed to provide an equivalent approximation to both regions. For this model space, we have obtained an effective Hamiltonian which produces good agreement for the observed level schemes of nuclei at and above ^{90}Zr and interesting predictions for the spectra of nuclei below ^{88}Sr.[1]

Many shell-model calculations in the $0g_{9/2}$-$1p_{1/2}$ model space have treated the nuclei above ^{90}Zr with considerable success.[2-8] The goal of our study in the expanded $N=50$ orbit space is to extrapolate this success down to lighter $N=50$ nuclei, recapitulating and modestly expanding the coverage of $N=50$ spectra above ^{90}Zr, explaining the complexities of the transition from the $0g_{9/2}$ region to the $0f_{5/2}$, $1p_{3/2}$, $1p_{1/2}$ region which takes place through the nuclei ^{90}Zr, ^{89}Y, and ^{88}Sr, and, finally, providing a guide to the spectra and structures of the nuclei lighter than ^{88}Sr. This approach thus follows in the line of publications which study the effects of adding additional orbits to the $1p_{1/2}$-$0g_{9/2}$ space. Early attempts explored limited expansions,[9-12] while other ongoing studies[13,14] use comparable or even larger spaces for ^{90}Zr and adjacent nuclei than the ones employed here. The empirically determined effective interaction of Ref. 1 yields energy-level predictions for nuclei above ^{90}Zr which are equivalent to earlier results in terms of agreement with experiment. Agreement with experimental energies for ^{90}Zr and lighter nuclei is not as accurate as that obtained for the $(g_{9/2})^n$ region, but there are no comparable theoretical results with which to compare the present predictions. In order to evaluate the new model results more thoroughly than is possible with only energy-level comparisons, the model wave functions must be used to generate predictions for other spectroscopic observables.

In the present paper we use the wave functions from this model and its Hamiltonian to calculate one-body spectroscopic amplitudes for multipole operators. From these values, and from the conventional assumptions about the forms of the electric quadrupole and magnetic dipole and hexadecupole operators, we predict values of $B(E2)$ for transitions and the electric quadrupole and magnetic dipole moments of some $N=50$ states, along with values of $M4$ transition strengths. These predictions are compared with existing experimental data in order to evaluate both the overall degree to which the model encompasses these observed phenomena and to determine the state-by-state consistency of the experimental-theoretical relationships. The electric quadrupole observables should illuminate the shape-collective features of the wave functions, while the magnetic dipole results reflect more the dominant single-particle structures of the states. The $M4$ results bear on the details of the occupancy of the $1p_{1/2}$ and $0g_{9/2}$ orbits in the transition region. Finally, we have used our model wave functions for ^{90}Zr to calculate the transition-charge densities for the yrast states of spins 2^+, 4^+, 6^+, and 8^+, and compared these predictions to results of recent electron scattering experiments.[14-16]

II. ELECTRIC QUADRUPOLE OBSERVABLES

We use the conventional definitions and assumptions[17] for the electric multipole operator $O(E,LM)$, namely,

$$O(E,LM)=\int \rho(\mathbf{r})r^L Y_{LM}(\theta,\phi)d\mathbf{r} = \sum_k e(k)r_k^L Y_{LM}(\theta_k,\phi_k) , \quad (1)$$

where $\rho(\mathbf{r})$ is the charge-density operator and $e(k)$ is the charge of the kth nucleon. The reduced transition rate $B(EL)$ for an electric Lth pole transition from an initial state $|J_iM_i\rangle$ to a final state $|J_fM_f\rangle$ is defined by

$$B(EL)=\frac{\langle J_f\|O(E,L)\|J_i\rangle^2}{2J_i+1} , \quad (2)$$

where the double vertibar indicates reduction with respect to angular momentum. The spectroscopic quadrupole moment of the state $|J,M=J\rangle$ is defined by

$$Q_2=\left[\frac{16\pi}{5}\right]^{1/2}\langle JJ|O(E,20)|JJ\rangle = \left[\frac{16\pi}{5}\right]^{1/2}\left[\frac{J(2J-1)}{(2J+1)(J+1)(2J+3)}\right]^{1/2} \times\langle J\|O(E2)\|J\rangle . \quad (3)$$

Thus shell-model predictions for electric transition rates and electric multipole moments of a nuclear system require calculations of the reduced matrix elements of the $O(EL)$ operators between the many-body shell-model wave functions. These matrix elements are obtained by expanding the $O(EL)$ operators in second-quantized form, using single-particle basis states $|j\rangle=a_j^\dagger|0\rangle$:

$$O(E,LM)=\sum_{j,j'}\frac{(a_j^\dagger\tilde{a}_{j'})^{LM}}{\sqrt{2L+1}}\langle j\|O(EL)\|j'\rangle . \quad (4)$$

Here j and j' are the quantum numbers specifying the single-particle states which define the shell-model basis. The coefficients $\langle j\|O(EL)\|j'\rangle$ are the elementary reduced single-particle matrix elements of the $O(EL)$ operators. From expression (4) it is clear that the state-dependent many-body aspects of the shell-model results are contained in the matrix elements of the $(a_j^\dagger\tilde{a}_{j'})^{LM}$ operators between initial and final shell-model wave functions. These matrix elements are independent of the detailed forms of the single-particle wave functions and are called one-body spectroscopic amplitudes, denoted in the following by $D_{j,j'}^{J_f,J_i}(L)$:

$$D_{j,j'}^{J_f,J_i}(L)=\left\langle J_f\left|\left|\frac{(a_j^\dagger\tilde{a}_{j'})^L}{\sqrt{2L+1}}\right|\right|J_i\right\rangle . \quad (5)$$

Combining the spectroscopic amplitudes with the single-particle matrix elements $S_{jj'}$ of the operators, where

$$S_{jj'}=\langle j||O(EL)||j'\rangle ,$$

we arrive at the final shell-model expression for reduced transition strengths,

$$B(EL)=\frac{\left[\sum_{j,j'}D_{j,j'}^{J_f,J_i}(L)S_{jj'}\right]^2}{2J_i+1} , \quad (6)$$

and similarly for multipole moments. This same form of expression also applies for the magnetic multipole matrix elements to be discussed in Secs. III and IV.

For shell-model wave functions which involve only one or two single-particle orbits, spectroscopic amplitudes can be calculated using simple formulas involving fractional parentage coefficients and Racah coefficients.[17] Calculations of spectroscopic amplitudes involving many shell couplings are only done practically with shell-model computer codes, such the RITSSCHIL code[18] used in the present work. For $E2$ transitions and moments there are nine nonzero spectroscopic amplitudes in the present model space, specifically those formed by the $0g_{9/2}$-$0g_{9/2}$, $1p_{1/2}$-$1p_{3/2}$, $1p_{1/2}$-$0f_{5/2}$, $1p_{3/2}$-$1p_{1/2}$, $1p_{3/2}$-$1p_{3/2}$, $1p_{3/2}$-$0f_{5/2}$, $0f_{5/2}$-$1p_{1/2}$, $0f_{5/2}$-$1p_{3/2}$, and $0f_{5/2}$-$0f_{5/2}$ single-particle creation-annihilation pairs. Note that the transitions of a conjugate pair, such as $1p_{1/2}$-$1p_{3/2}$ and $1p_{3/2}$-$1p_{1/2}$, should have different amplitudes unless the initial and final nuclear states are identical.

The single-particle matrix elements for the $O(EL)$ operator can be factored into radial and angular parts,

$$\langle nl_j\|r^L Y_{LM}(\mathbf{r})\|n'l'j'\rangle=\langle nl|r^L|n'l'\rangle f_L(j,j') . \quad (7)$$

The radial integrals used in the present work are calculated with the harmonic-oscillator wave functions. The calculated values of $f_2(j,j')$ and $\langle r^2\rangle$ used here for $N=50$ nuclei are listed in Table I, along with the single-particle matrix elements for the $E2$ operator calculated using Eq. (7).

Predictions for $B(E2)$ values of $N=50$ nuclei are calculated from our shell-model wave functions according to formula (6). The results are presented in Table II. The $B(E2)_{\text{free}}$ values in Table II are calculated with a proton charge equal to $1.0e$. In comparison with the experimental data, these $B(E2)_{\text{free}}$ values are systematically too small, as is expected. We adopt the conventional "effective charge" model to renormalize the "free nucleon" $E2$ predictions for the effects of excluded configurations. In principle, effective charges can be different for different states, different nuclei, and different single-particle orbits. The present results are based on the minimalist assumption that the effective charge is the same for all states, all $N=50$ nuclei and all model orbits, specifically, $e_p=2.0e$. The predictions based on this effective $E2$ operator are listed in the $B(E2)_{\text{eff}}$ column of Table II. As a partial aid to evaluating the effects of configuration mixing within our model space upon the calculated electric quadrupole matrix elements, we show in comparison with $B(E2)_{\text{free}}$ the corresponding values obtained with one-component wave functions given by the simplest possible shell-model configuration, denoted as $B(E2)_{\text{ncm}}$.

The $E2$ data with which we compare our results in Table II are taken from Refs. 19–25. The $B(E2)$ values for the transitions from the first 2^+ state to ground state 0^+, both calculated and, where measured, experimental,

TABLE I. Single-particle matrix elements calculated for the $E2$ and $M1$ operators for the orbits $|j\rangle$ and $|j'\rangle$ with the free-proton charge and magnetic moment. The expressions $f_2(j,j')$ and $\langle r^2\rangle$ are as defined in Ref. 17. The values of the $E2$ matrix elements are calculated with the assumption that the harmonic-oscillator length parameter is given by $b^2=4.481$.

j,j'	$f_2(j,j')$	$\langle r^2\rangle$	$\langle j\|\|O(E2)\|\|j'\rangle$	$\langle j\|\|\mathbf{L}\|\|j'\rangle$	$\langle j\|\|\mathbf{S}\|\|j'\rangle$	$\langle j\|\|O(M1)\|\|j'\rangle$
$f_{5/2}$-$f_{5/2}$	−0.739	$4.500b^2$	−14.905	8.281	−1.035	2.499
$f_{5/2}$-$p_{3/2}$	−0.369	$-3.742b^2$	6.189	0.000	0.000	0.000
$f_{5/2}$-$p_{1/2}$	0.691	$-3.742b^2$	−11.589	0.000	0.000	0.000
$p_{3/2}$-$p_{3/2}$	−0.564	$4.500b^2$	−11.374	2.582	1.291	9.794
$p_{3/2}$-$p_{1/2}$	−0.564	$4.500b^2$	−11.374	1.155	−1.155	−5.297
$p_{1/2}$-$p_{1/2}$	0.000	$0.000b^2$	0.000	1.633	−0.408	0.646
$g_{9/2}$-$g_{9/2}$	−0.982	$5.500b^2$	−24.204	13.98	1.748	23.74

are large, as is typical. The theoretical values with the effective proton charge of 2.0e are in overall agreement with the data. The ^{86}Kr and ^{88}Sr $B(E2)_{\text{eff}}$ values are each about two standard deviations smaller than the quoted experimental values. The measured decrease in strength from $A=86$ to 88 is 11%, while the predicted decrease is 22%. The measured $B(E2)$ for ^{90}Zr 2_1^+ to 0_1^+ is almost a factor of 2 smaller than the ^{86}Kr value, and the prediction for ^{90}Zr lies within the uncertainty of the experimental value. Thus the observed decrease in strength between ^{86}Kr and ^{90}Zr is reproduced accurately by the calculations. The ^{92}Mo strength for this transition is significantly larger than for ^{90}Zr, and is approximately the same as for ^{88}Sr. The predicted $B(E2)_{\text{eff}}$ value for ^{92}Mo is essentially equal to the measured value.

The ^{92}Mo, ^{94}Ru, and ^{96}Pd transitions are dominated by the $0g_{9/2}$ 2^+ to 0^+ one-body transition, while the ^{86}Kr and ^{88}Sr transitions are dominated by one-body transitions within the $1p_{3/2}$-$1p_{1/2}$ subspace. The reduction in $B(E2)$ which is observed and predicted for ^{90}Zr can be understood in terms of contributions from both these paths, contributions which partially cancel.

There are several other accurately measured $B(E2)$ values in ^{92}Mo, as shown in Table II, ranging in magnitude from about 1 to 100 e^2fm^4. The $B(E2)_{\text{eff}}$ predictions are uniformly in good agreement with these accurate experimental numbers, the discrepancy for the 6^+-4^+ transition being the largest. These results suggest that the effective charge of 2.0e is close to optimum for the $0g_{9/2}$ part of our model space and that the model wave functions for the several other ^{92}Mo states sampled are good representations of their physical analogs. Similar results with similar conclusions are manifest in the cases of the $\frac{21}{2}^+$ to $\frac{7}{2}^+$ transitions in ^{91}Nb and ^{93}Tc. The predicted $B(E2)$ of the $\frac{17}{2}^-$ to $\frac{13}{2}^-$ transition in ^{91}Nb is also in good agreement with experiment, but the predicted strength for the analogous transition in ^{93}Tc is much too large.

Two electric quadrupole moments have been measured for $N=50$ states, the $\frac{3}{2}^-$ ground state of ^{87}Rb and the first 8^+ state of ^{90}Zr. The value of $Q2_{\text{eff}}$ for each state is larger than experiment by 25%. The wave functions of these states are quite simple, the ^{87}Rb wave function being predominantly a $1p_{3/2}$ single-particle state and the ^{90}Zr state a $0g_{9/2}$ pair coupled to 8^+. The calculated matrix elements are enhanced over the single-particle estimates by 10% and 20%, respectively. The signs of both the simple configuration estimates and the full calculation are in agreement with experimental values.

There are only a few other $B(E2)$ measurements available. The strength of the transition between the first excited state ($J^\pi=\frac{3}{2}^-$) to ground state ($J^\pi=\frac{5}{2}^-$) in ^{87}Rb is accurately known, and our $B(E2)_{\text{eff}}$ reproduces it closely. This transition and the two ground-state transitions in ^{89}Y are the only other sources of information on the electromagnetic properties of the $0f1p$ subspace. The assumed value of 2.0e for the effective charge seems optimum for this subset overall.

The $E2$ relationships between the first 2^+ state and the ground state and first excited 0^+ states in ^{90}Zr, in which the excited state 0^+ $B(E2)$ is larger than the ground-state 0^+ value, are well reproduced by the model results. The calculated $B(E2)$ values for the transitions from the second and third 2^+ states to the ground-state 0^+ are markedly wrong, however. If anything, the calculations suggest that the second and third model states may be inverted in energy relative to their experimental analogs.

The last significant set of $E2$ data available for the $N=50$ isotones comprises the 8^+ to the 6^+ decays. The measured value for ^{90}Zr is predicted accurately. The model also does a good job of predicting the noticeably smaller value of the same transition in ^{92}Mo. The predicted $B(E2)$ value for this transition in ^{96}Pd is about one-quarter of the ^{92}Mo value, and the measured value is in a nice correspondence with the prediction. Finally, the $B(E2)$ of the 8^+ to 6^+ transition in ^{94}Rb is dramatically smaller than in the neighboring systems. The predicted value is about 50 times smaller than the value in ^{92}Mo, and the measured strength is ten times smaller yet. We do not attach great significance to the relative discrepancy between prediction and experiment in this last case, since the absolute difference is so small relative to the single-particle value. Small adjustments in the wave function can account for this difference.[7]

III. MAGNETIC DIPOLE MOMENTS

The magnetic charge density $\rho_m(\mathbf{r})$ of a nucleus comes from the orbital motion of the charged particles, i.e., the convection currents, $\rho_c(\mathbf{r})$, and the magnetic moments associated with spins of the individual nucleons, $\rho_s(\mathbf{r})$. The magnetic multipole moment operators can be defined

TABLE II. $E2$ transitions and moments in units of $e^2\text{fm}^4$ or $e\text{fm}^2$ for the $N=50$ nuclei, respectively. The values in the $B(E2)_{\text{eff}}$ column are obtained with the proton effective charge $e_p=2.0e$. The values in the column $B(E2)_{\text{free}}$ are obtained with the free-space proton charge $e_p=1.0e$. The values in the column $B(E2)_{\text{ncm}}$ are obtained with wave functions consisting of the basis vectors that have the largest magnitude in the corresponding eigenvectors, i.e., in the limit of no configuration mixing.

Nucleus	State (s)	$B(E2)_{\text{expt}}$	$B(E2)_{\text{eff}}$	$B(E2)_{\text{free}}$	$B(E2)_{\text{ncm}}$
^{86}Kr	$2_1^+\rightarrow 0_1^+$	256±20[a]	212	53.1	52
	$4_1^+\rightarrow 2_1^+$		29.4	7.4	7.3
	$6_1^+\rightarrow 4_1^+$		25.8	6.4	9.0
^{87}Rb	$\frac{3}{2}_1^-$	13±0.5[b]	17.6	8.8	8.0
	$\frac{5}{2}_1^-\rightarrow\frac{3}{2}_1^-$	36.6±0.6[c]	42.8	10.7	12.8
	$\frac{1}{2}_1^-\rightarrow\frac{3}{2}_1^-$		83.1	20.8	64
^{88}Sr	$2_1^+\rightarrow 0_1^+$	228±30[a]	166	41.4	52
	$4_1^+\rightarrow 2_1^+$		50.8	12.7	45
	$6_1^+\rightarrow 4_1^+$		114	28.5	0.0
^{89}Y	$\frac{3}{2}_1^-\rightarrow\frac{1}{2}_1^-$	66±10[c]	76.8	19.2	64
	$\frac{5}{2}_1^-\rightarrow\frac{1}{2}_1^-$	66±5[c]	38.8	9.7	0.0
	$\frac{5}{2}_1^+\rightarrow\frac{9}{2}_1^+$	283±118[c]	90	22.5	52
	$\frac{13}{2}_1^+\rightarrow\frac{9}{2}_1^+$		142	35.4	52
^{90}Zr	$2_1^+\rightarrow 0_1^+$	135±12[d]	122	30.5	0.0
	$2_1^+\rightarrow 0_2^+$	150±13[d]	173	43.2	0.0
	$2_2^+\rightarrow 0_1^+$	13.4±2[c]	91	22.7	0.0
	$2_3^+\rightarrow 0_1^+$	40.7±7[c]	1.8	0.44	0.0
	$4_1^+\rightarrow 2_1^+$		260	64.9	106
	$6_1^+\rightarrow 4_1^+$		188	47.1	74
	$8_1^+\rightarrow 6_1^+$	55±2[c]	54.4	13.6	30
	8_1^+	−51±3[e]	−61.3	−30.7	−24
	$10_1^+\rightarrow 8_1^+$		3.0	0.76	0.0
^{91}Nb	$\frac{21}{2}_1^+\rightarrow\frac{17}{2}_1^+$	106±11[d]	126	31.5	59
	$\frac{17}{2}_1^+\rightarrow\frac{13}{2}_1^+$		311	77.7	102
	$\frac{13}{2}_1^+\rightarrow\frac{9}{2}_1^+$		118	29.5	0.0
	$\frac{17}{2}_1^-\rightarrow\frac{13}{2}_1^-$	32.0±1.9[d]	25.6	6.4	30
	$\frac{13}{2}_1^-\rightarrow\frac{9}{2}_1^-$	71.1±3.2[d]	120	30.1	74
	$\frac{9}{2}_1^-\rightarrow\frac{5}{2}_1^-$	≤178[d]	222	55.5	106
	$\frac{5}{2}_1^-\rightarrow\frac{1}{2}_1^-$	144±72[c]	238	59.5	92
^{92}Mo	$2_1^+\rightarrow 0_1^+$	234±40[d]	237	59.3	92
	$2_2^+\rightarrow 0_1^+$	47.6±3.2[c]	47.6	11.9	0.0
	$2_3^+\rightarrow 0_1^+$	2.0±0.7[c]	1.4	0.35	0.0
	$2_4^+\rightarrow 0_1^+$	37±10[c]	43.6	10.9	0.0
	$4_1^+\rightarrow 2_1^+$		115	28.7	106
	$6_1^+\rightarrow 4_1^+$	78.5±2.5[d]	96	24.0	74
	$8_1^+\rightarrow 6_1^+$	32.4±1.2[d]	38.4	9.6	30
	$10_1^+\rightarrow 8_1^+$		89	22.2	0.0
	$12_1^+\rightarrow 10_1^+$		268	66.9	80
	$11_1^-\rightarrow 9_1^-$	85±5[d]	91.2	22.8	59
	$9_1^-\rightarrow 7_1^-$		194	48.6	102
	$7_1^-\rightarrow 5_1^-$		268	66.9	105
^{93}Tc	$\frac{21}{2}_1^+\rightarrow\frac{17}{2}_1^+$	65.9±4.0[d]	78.4	19.6	109
	$\frac{17}{2}_1^+\rightarrow\frac{13}{2}_1^+$		126	31.5	102
	$\frac{13}{2}_1^+\rightarrow\frac{9}{2}_1^+$		238	59.6	105
	$\frac{17}{2}_1^-\rightarrow\frac{13}{2}_1^-$	11.4±0.9[d]	59.6	14.9	3.2
	$\frac{5}{2}_1^-\rightarrow\frac{1}{2}_1^-$		304	76	139

TABLE II. (*Continued.*)

Nucleus	State (s)	$B(E2)_{expt}$	$B(E2)_{eff}$	$B(E2)_{free}$	$B(E2)_{ncm}$
^{94}Ru	$2_1^+ \rightarrow 0_1^+$		282	70.4	139
	$4_1^+ \rightarrow 2_1^+$		2	0.53	11.8
	$6_1^+ \rightarrow 4_1^+$	2.56±0.24[d]	6	1.51	8.2
	$8_1^+ \rightarrow 6_1^+$	0.094±0.006[d]	0.9	0.23	3.2
	$10_1^+ \rightarrow 8_1^+$	≥3.6[f]	209	52.4	108
	$12_1^+ \rightarrow 10_1^+$	81.2±7.6[f]	104	26	80
	$7_1^- \rightarrow 5_1^-$		36.8	92.1	140
	$9_1^- \rightarrow 7_1^-$		42.7	106.7	170
	$11_1^- \rightarrow 9_1^-$	71.0±12.7[f]	333	83.3	140
	$13_1^- \rightarrow 11_1^-$	≥64.2[f]	298	74.6	138
^{95}Rh	$\frac{13}{2}_1^+ \rightarrow \frac{9}{2}_1^+$		262	65.4	140
	$\frac{17}{2}_1^+ \rightarrow \frac{13}{2}_1^+$		11	2.7	0.0
	$\frac{21}{2}_1^+ \rightarrow \frac{17}{2}_1^+$	33±5.0[f]	0.02	0.005	0.0
	$\frac{25}{2}_1^+ \rightarrow \frac{21}{2}_1^+$	≥7.5[f]	152	38	138
	$\frac{21}{2}_1^- \rightarrow \frac{17}{2}_1^-$		357	89.2	108
	$\frac{25}{2}_1^- \rightarrow \frac{21}{2}_1^-$	163±25.4[f]	247	61.8	80
^{96}Pd	$2_1^+ \rightarrow 0_1^+$		254	63.5	139
	$4_1^+ \rightarrow 2_1^+$		43	10.8	11.8
	$6_1^+ \rightarrow 4_1^+$	13±3[g]	22	5.4	8.2
	$8_1^+ \rightarrow 6_1^+$	8.6±1.1[g]	9	2.3	3.2
	$10_1^+ \rightarrow 8_1^+$		185	46.3	108
	$12_1^+ \rightarrow 10_1^+$		157	39.2	80

[a]Reference 19.
[b]Reference 20.
[c]Reference 21.
[d]Reference 22.
[e]Reference 23.
[f]Reference 24.
[g]Reference 25.

analogously to the electric multipole moment operators, namely,

$$O(M,LM)=\int \rho_m(\mathbf{r})r^L Y_{LM}(\theta,\varphi)d\mathbf{r}$$
$$=\sum_k \mu_N[\nabla_k r_k^L Y_{LM}(\theta_k,\phi_k)]$$
$$\times\left[\frac{2g_l(k)}{L+1}\mathbf{L}_k+g_s(k)\mathbf{S}_k\right], \quad (8)$$

where μ_N is the nuclear magneton and the sum over k includes all particles in the nucleus.

In this section, only the magnetic dipole operator is studied. The traditionally used dipole operator, which differs from the general expression in Eq. (8) by a numerical factor $\sqrt{3/4\pi}$, is given by

$$O(M1)=\sum_k [g_l(k)\mathbf{L}_k+g_s(k)\mathbf{S}_k], \quad (9)$$

where g_l and g_s are the nucleon gyromagnetic ratios. The magnetic moment in a state with total angular momentum J and maximum magnetic quantum number $M=J$ is defined as

$$\mu_1=\langle JJ|O(M1)|JJ\rangle$$
$$=\left[\frac{J}{(J+1)(2J+1)}\right]^{1/2}\langle J\|O(M1)\|J\rangle . \quad (10)$$

Thus, to obtain theoretical magnetic moments, we have to calculate the matrix elements of the $O(M1)$ operator between the multiparticle wave functions. Thus use of Eq. (6) again reduces this problem to the calculation of one-body spectroscopic amplitudes and single-particle matrix elements. The $M1$ single-particle matrix elements in our model space are listed in Table I along with the separate contributions from the orbital part and the spin part of the operator.

Experimental data[20,26] for $M1$ moments in $N=50$ nuclei are compared with various model predictions in Table III. The states for which magnetic moments have been measured are the ground states of ^{87}Rb, ^{89}Y, and ^{93}Tc, and 8^+ states of ^{90}Zr, ^{92}Mo, and ^{94}Ru, and 6^+ state of ^{94}Ru, the $\frac{13}{2}^-$ and $\frac{17}{2}^-$ states of ^{91}Nb, and the $\frac{17}{2}^-$ state of ^{93}Tc.

The simplest model estimate of a state's magnetic moment, obtained from the matrix elements of the single basis vector representing the dominant shell-model configuration of a state, is often a good approximation to the experimental value. We list these generalizations of the Schmidt moments in Table III as μ_{ncm}. It is clear from Table III that that μ_{ncm} numbers qualitatively explain the magnetic moment data, with the deviations in most cases being less than 15%. It is assumed that these deviations, which are always in the direction of theoretical magnitudes being larger than experimental values, arise from the effects of configurations omitted from

TABLE III. $M1$ moments for the $N=50$ nuclei in units of nuclear magnetons. The values listed under $\mu_{\rm ncm}$ are calculated with wave functions corresponding to the single dominant configuration of the full shell-model wave functions. The column $\mu_{\rm free}$ is obtained by using the full shell-model wave functions and the free-space g factors. The column $\mu_{\rm eff}$ shows the results calculated with the effective g factors obtained from the fit described in the text.

Nucleus	State (s)	$\mu_{\rm expt}$	$\mu_{\rm eff}$	$\mu_{\rm free}$	$\mu_{\rm ncm}$
^{87}Rb	$\frac{3}{2}^-$	2.751[a]	3.107	3.328	3.800
^{89}Y	$\frac{1}{2}^-$	−0.138[a]	−0.032	−0.229	−0.270
^{90}Zr	8^+	10.912[b]	10.854	11.553	12.08
^{91}Nb	$\frac{13}{2}^-$	8.190[a]	7.714	7.948	9.035
	$\frac{17}{2}^-$	10.854[b]	10.423	10.829	11.815
^{92}Mo	8^+	11.352[b]	11.229	12.028	12.08
	11^-	13.882[b]	13.910	14.559	15.587
^{93}Tc	$\frac{9}{2}^+$	6.151[a]	6.323	6.773	6.800
	$\frac{17}{2}^-$	11.059[b]	10.519	10.947	11.815
^{94}Ru	6^+	8.322[b]	8.435	9.040	9.060
	8^+	10.832[b]	11.247	12.051	12.08

[a]Reference 20.
[b]Reference 26.

Schmidt estimates, the net effect of configuration mixing typically being to quench Schmidt estimates.

Our present shell-model wave functions for these nuclear states represent an intermediate stage between the simple Schmidt estimate and the presumed "true" wave functions. In the $\mu_{\rm free}$ column of Table III we present predictions for the $M1$ moments based on the full configuration-mixed wave functions of our model space. These model predictions are still larger than the experimental values in most cases, but typically are smaller than the $\mu_{\rm ncm}$ values, particularly for the states dominated by $0f1p$ orbit configurations. In the cases dominated by the $0g_{9/2}$ configuration the $\mu_{\rm free}$ values are almost as large as the $\mu_{\rm ncm}$ values, since the $0g_{7/2}$ orbit, the spin-orbit partner of the $0g_{9/2}$ orbit, is not in our model space and hence cannot act to cancel contributions from $0g_{9/2}$ components in our wave functions.

To compensate for the effects of the various configurations omitted from our model space, we introduce effective spin and orbital g factors for the protons of our model, their values being determined by a least-squares fit to best reproduce the experimental data. In principle, we could imagine determining effective single-proton moments for each of the four orbits in our model space. (Even if in the complete $0f1p0g$ space these orbits had identical renormalizations, the fact that the spin-orbit partners of the $0f_{5/2}$ and $0g_{9/2}$ orbits are missing in our current space, while the $1p$-orbit subspace is complete, suggests that effective renormalizations might be orbit dependent in the present application.) However, the paucity of experimental data for the $N=50$ isotones which bear on the $0f1p$ orbits makes it rather pointless to push determination of their renormalization very hard. Most of the data bears on the $0g_{9/2}$ orbit alone and hence can fix only the $0g_{9/2}$ proton effective moment.

We hence have extracted the values of an $M1$ renormalization by fitting the data of Table III with adjustable values of $g_s(0f1p)$ and $g_s(0g_{9/2})$ while fixing $g_l(0f1p0g)$ at the value 1.10 (Ref. 27). This value of g_l (effective) is found rather universally in analyses of magnetic-moment data with shell-model wave functions. It is understood in terms of mesonic-exchange currents. From this fit, we obtain the value $g_s(0f1p)_{\rm eff}=4.694$ and $g_s(0g_{9/2})_{\rm eff}=3.953$. The larger quenching for $g_s(0g_{9/2})$ is consistent with the fact that our space omits the spin-orbit partner of this orbit, and hence configuration mixing to quench its impact is impossible. The values of magnetic moments predicted with this empirical effective operator are presented in the $\mu_{\rm eff}$ column of Table III.

The ground states of ^{87}Rb, ^{89}Y, and ^{93}Tc are essentially single-particle states. The Schmidt estimates are larger than the experimental value by 38%, 96%, and 11%, respectively. The configuration-mixing shell-model wave functions bring the discrepancies down to 21%, 66%, and 10%. Again, we note that configuration mixing in our model space has only a very small effect upon the moments of states dominated by the $0g_{9/2}$ orbit.

The 6^+ and 8^+ states in ^{90}Zr, ^{92}Mo, and ^{94}Ru are essentially two quasiparticles in the $0g_{9/2}$ orbit. The Schmidt g factors are the same for all these states. Their experimental g factors are equal to each other to within 4%, and are smaller than the Schmidt values by 7–10%. The configuration-mixing calculations produce results essentially equal to the Schmidt values of ^{92}Mo and ^{94}Ru, but reduce the discrepancy in ^{90}Zr by half.

The three-quasi-particle $\frac{13}{2}^-$ and $\frac{17}{2}^-$ states in ^{91}Nb and ^{93}Tc have the same first-order configuration and so have the same Schmidt g factors. The measured g factors for these states increase with the mass, however. This is because the configuration mixing decreases as the number

of particles in the $g_{9/2}$ orbit increases. Our configuration-mixing calculation eliminates the discrepancies between the measured data and the Schmidt predictions.

Theoretical understanding of the quenching of g factors has been a major subject of study for many years.[27] Finite shell-model spaces in theoretical calculations such as we utilize in this work still exclude many other possible configurations, both nucleonic and non-nucleonic. These extra degrees of freedom include meson-exchange currents, nucleonic excitations, and mixings with much higher-lying shell-model orbits induced by the tensor force. Hence our effective g factors must be considered as representing the net empirical representation of this complex of causes. Theoretical calculations of the effects of these fundamental processes agree with the empirical extractions reasonably well.[27]

IV. MAGNETIC HEXADECUPOLE TRANSITIONS

The juxtaposition of the $1p_{1/2}$ and $0g_{9/2}$ orbits above ^{88}Sr gives rise to a series of isometric first excited states in the odd-mass $N=50$ nuclei, $\frac{9}{2}^+$ for ^{89}Y and $\frac{1}{2}^-$ for ^{91}Nb, ^{93}Tc, and ^{95}Rh. These first excited states decay in part by $M4$ transitions to the ground states of the same nuclei and the matrix elements of these transitions yield interesting insight into the makeup of the associated wave functions, particularly insofar as the mixing of $0g_{9/2}$ and $1p_{1/2}$ orbits is concerned.

The general form of the magnetic multipole operators is given in Eq. (8). This expression yields values of the $M4$ single-particle matrix elements equal to 2091 μ_N^2 fm^6 for $1p_{1/2}$-$0g_{9/2}$, 2134 μ_N^2 fm^6 for $1p_{3/2}$-$0g_{9/2}$, and 1256 μ_N^2 fm^6 for $0f_{5/2}$-$0g_{9/2}$. These values combined with the one-body transition densities from the current shell-model wave functions yield the predictions labeled "free" in Table IV. They are compared in Table IV with experimental data taken from Ref. 20. Also presented in Table IV are predictions obtained by multiplying the free values by a scale factor of 0.223, these renormalized results being labeled as "eff." Finally, in order to illustrate the role of configuration mixing we show the predictions, labeled "ncm," obtained by combining the free single-particle matrix elements with the one-body densities associated with the dominant shell-model basis vector in each eigenvector, these dominant components being renormalized to unit amplitudes.

As is seen from Table IV, the experimental magnitudes of the matrix elements for the $M4$ transitions are rather similar, the value for ^{95}Rh being about twice as large as the ^{89}Y and ^{91}Nb values. The "free" predictions are about a factor of 5 larger than the experimental values, but the renormalized "eff" values yield a reasonably accurate reproduction of the experimental trends as a function of mass. The effects of configuration mixing in our calculation are crucial in obtaining this correct mass dependence, as can be seen from the "ncm" results. If wave functions corresponding to the leading $1p_{1/2}$ and $0g_{9/2}$ configurations are used, the single-particle $0g_{9/2}$ to $1p_{1/2}$ transition in ^{89}Y has twice as large a matrix element as any of the higher mass transitions and a factor of 5 larger matrix element than that of the $1p_{1/2}\otimes 0g_{9/2}^2 - 1p_{1/2}^2\otimes 0g_{9/2}$ transition in ^{91}Nb. As a result of configuration mixing the ^{89}Y prediction is reduced, since neither of the wave functions involved remains a pure single-particle state, while the higher mass predictions, particularly that for ^{91}Nb, are increased via positively coherent contributions from the $1p_{1/2}^{-2}$ configurations. The decreasing amplitudes of these components as a function of increasing mass accounts for the diminishing enhancement of the "free" results over the "ncm" results with increasing mass.

The quenching mechanism for the magnetic hexadecupole operator is similar to that for the magnetic dipole operator discussed in Sec. III. However, detailed study of the importance of various contributions is very rare to date, both because of the paucity of experimental data and of the complicated structure of the $M4$ operator. More theoretical work is certainly called for to obtain a qualitative understanding of the strong quenching seen in the present calculations.

V. CHARGE TRANSITION DENSITIES

Electron scattering cross sections at both low and high momentum transfers $|\mathbf{q}|$ can be measured very accurately with modern experimental techniques. By analyzing experimental cross sections at various values of $|\mathbf{q}|$ with the distorted-wave Born approximation (DWBA) theory, the transition charge, moment, and current densities at different spatial points can be determined. Unlike transition rates and moments, measured in the context of $|\mathbf{q}|=\omega\approx 0$, for which only the integrated charge or

TABLE IV. Matrix elements $M(M4)=(2J_i+1)B(M4)$ in terms of μ_N^2 fm$^6\times 10^5$ for $N=50$ nuclei. The experimental data are taken from Ref. 20. The values listed under $M_{\rm ncm}$ are calculated with the free-space normalization of the $M4$ operator and wave functions corresponding to the single dominant component of the full shell-model wave function, and the values listed under $M_{\rm free}$ are calculated with the same operator and the full shell-model wave function. The values $M_{\rm eff}$ are obtained simply by multiplying the $M_{\rm free}$ values by 0.223.

Nucleus	Transition	$M_{\rm expt}$	$M_{\rm eff}$	$M_{\rm free}$	$M_{\rm ncm}$
^{89}Y	$\frac{9}{2}^+_1 \rightarrow \frac{1}{2}^-_{\rm g.s.}$	5.3	6.7	30.0	44.0
^{91}Nb	$\frac{1}{2}^-_1 \rightarrow \frac{9}{2}^+_{\rm g.s.}$	5.2	6.0	26.8	8.8
^{93}Tc	$\frac{1}{2}^-_1 \rightarrow \frac{9}{2}^+_{\rm g.s.}$	8.2	7.8	34.4	17.4
^{95}Rh	$\frac{1}{2}^-_1 \rightarrow \frac{9}{2}^+_{\rm g.s.}$	10.6	8.6	38.4	26.0

current densities are relevant, these transition densities thus provide spatially extended nuclear information and thus invoke extra challenges to any nuclear model. In addition, electron scattering makes practical the study of transition multipolarities which are unobservable in electromagnetic decay because of preferred competing decay modes. We concentrate here on transition-charge densities, which are related to the so-called Coulomb (or longitudinal) scattering cross sections in electron scattering.

In the nuclear shell model, the transition-charge densities can be calculated in terms of single-particle transition densities in a fashion analogous to Eq. (6). Explicitly, they can be written as the sum of contributions from the different pairs of orbital transitions,[28]

$$\rho_v^L(r)=\sum_{j,j'}\frac{D_{j,j'}^{J_f,J_i}(L)R_j(r)R_{j'}(r)\langle j\|Y_L\|j'\rangle}{\sqrt{2J_f+1}}\ , \tag{11}$$

where the $R_j(r)$ are the single-particle wave functions, the $D_{j,j'}^{J_f,J_i}(L)$ are the spectroscopic amplitudes identified in Eq. (5) and J_f and J_i are the spins of the final and initial nuclear states. In principle, the sum must extend over all possible routes of single-particle transitions, but the shell-model approximation restricts this sum to the active model orbits. Thus the densities calculated using Eq. (11) within finite model spaces are called "valence" transition densities.

Comparison of valence transition densities with experimental results reveals that the configurations excluded from the active model space typically have significant "core-polarization" effects upon the overall magnitudes, as is also the case, of course, for transition rates and moments. For transition densities, the core-polarization effects are more complicated than for $q=0$ data because their radial dependences must be considered. Four different kinds of radial dependences are commonly used for parametrizing the core-polarization densities.[29] The first is the so-called "valence" model, in which the core-polarization transition densities are assumed to have the same radial dependences as the corresponding valence transition densities:

$$\rho_c^L(r)=a\rho_v^L(r)\ , \tag{12}$$

where a is a constant of proportionality. The second is the Tassie model, for which the radial dependence is

$$\rho_c^L(r)=ar^{L-1}\frac{d\rho_0}{dr}\ , \tag{13}$$

where ρ_0 is the ground-state density. The third is the Bohr-Mottelson model, in which the radial dependence is

$$\rho_c^L(r)=a\frac{d\rho_0}{dr}\ . \tag{14}$$

A fourth general type of core polarization has microscopic origins. The amplitudes of single-particle transitions from orbits lying outside the model space are calculated in perturbation theory and used directly with the nucleon charges and moments to estimate the core-polarization term.

The total transition density can be written as a sum of the valence contribution and the core-polarization contribution,

$$\rho_t^L(r)=\rho_v^L(r)+\rho_c^L(r)\ . \tag{15}$$

The coefficient a of the core-polarization term is typically adjusted such that the experimental electric transition rate for the transition is reproduced. Of course, if the experimental rate is unavailable, some other normalization must be used. For higher multipolarities one simple technique is to match the theoretical and experimental first maxima of the form factors. Of course, a primary virtue of the microscopic core-polarization models is that they do not involve an additional parameter at this point.

In principle, the single-particle wave functions used in the calculations of transition densities should be calculated from potentials of the Woods-Saxon or Hartree-Fock type, because the radial dependence of these wave functions may be critical to the radial structure of the transition densities. However, these more complicated wave functions do not necessarily provide better agreement between theory and experiment than do simple harmonic-oscillator wave functions, at least for light nuclei. Thus, for simplicity, we use harmonic-oscillator single-particle wave functions in the following calculations. The oscillator length parameter b is chosen to be 2.2 fm on the basis of obtaining agreement between predictions and experiment for the peak position of 8^+ state density of the ^{90}Zr nucleus. This value is a little larger than the value required to reproduce the charge rms radius of ^{90}Zr. The shell-model transition densities calculated from Eq. (15) must be modified for comparison with experimental results in order to correct them for the effects of finite nucleon size and center-of-mass motion. We make these corrections according to the prescription of Ref. 28.

As examples of the application of our shell-model wave functions to electron scattering data, we treat the experimental transition densities presented in Ref. 14 for the transitions from the ground state of ^{90}Zr to the $J=2^+$, 4^+, 6^+ and 8^+ members of the presumed $0g_{9/2}^2$ multiplet. Under this presumption, these states would be populated via excitation of the $0g_{9/2}^2$ component of the ^{90}Zr ground state.

We discuss the 8^+ transition first, since it can only be reached by a $0g_{9/2}$ transition within the model space and other high-spin orbits are relatively remote. The $0g_{9/2}^2$ spectroscopic amplitude which governs this transition has a calculated value of 0.406, reflecting the strong mixing between the $1p_{1/2}^2$ and $0g_{9/2}^2$ configurations in the ^{90}Zr ground state. An analysis of the 8^+ data in Ref. 28 yields a value of 0.41 ± 0.02 for this quantity.

It follows, as in shown in Fig. 1, that the calculated 8^+ transition density is a good approximation to the experimental results. The peak of the density is a factor of 0.92 times the experimental density. This is reflected in a peak value in the form factor [calculated in the plane-wave Born approximation (PWBA)], occurring at $q=1.8$ fm^{-1}, of 4.21×10^{-3}, relative to an experimental value of 5.00×10^{-3}. An enhancement of 1.09 in the valence transition density serves to bring theoretical and experimental agreement for the maximum values of both the transition densities and the form factors. The theoretical shape of

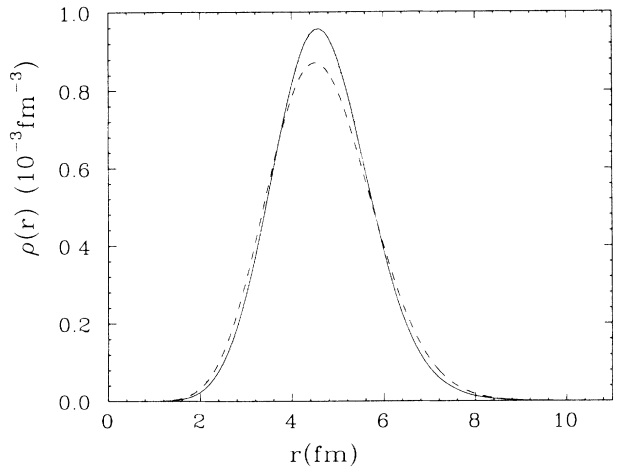

FIG. 1. Charge density from the first 0^+ to the first 8^+ transition in the ^{90}Zr nucleus. The dashed line represents the valence density calculated in the present model. The dotted line represents the total transition density in the valence core-polarization model. The solid line is the experimental density taken from Ref. 14.

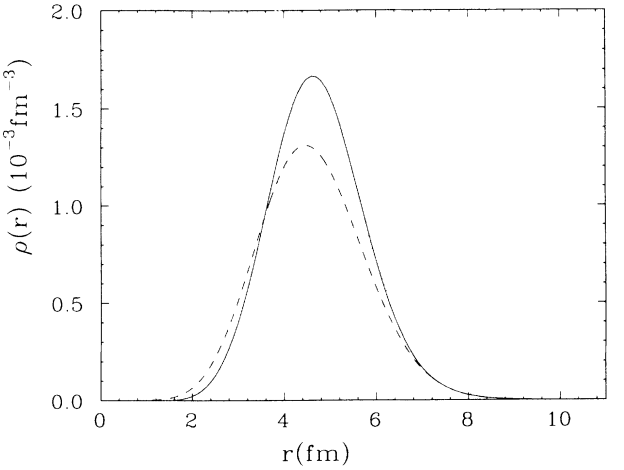

FIG. 2. Charge densities from the first 0^+ to the first 6^+ transition in the ^{90}Zr nucleus. Different curves have the same meaning as in Fig. 1.

the density agrees well with experiment. Hence we conclude that the valence model for core polarization is adequate for $E8$ transitions and that the required effective added charge is small, less than $0.1e$. Of course, the value extracted for the effective charge is a function of the predicted one-body transition amplitude, and a value slightly larger than 0.406 would result in the deduced effective charge being zero or even negative.

Analyses[30] of the experimental data for the 8^+ transitions in ^{88}Sr and ^{92}Mo have resulted in extracted values for the $E8$ spectroscopic factor of 0.36 ± 0.02 and 0.58 ± 0.02, respectively, as compared to our predictions of 0.145 and 0.658. The deviations between our predictions and these experimental results are comparable to those quoted for other shell-model calculations in Refs. 14 and 30. Analysis of our wave functions for ^{88}Sr suggests that a significant reason for our predicted ^{88}Sr density being too small is that only about 50% of our lowest ^{88}Sr 8^+ wave function can be characterized as the $0g^2_{9/2}$ two-particle state, not just that the $0g_{9/2}$ occupation in the ground state is too small.

Our model predictions for the first 6^+ transition in ^{90}Zr are similar to those for the 8^+; the results are shown in Fig. 2. The shell-model density is smaller than the experimental density by a factor of 0.81 in the region of the peak. An effective charge of 1.23 in the valence core-polarization model serves to normalize the peak theoretical density to the experimental peak value and to produce a PWBA form factor with a maximum value, occurring at 1.4 fm^{-1}, of 2.0×10^{-2}, which also matches the experimental value.[14]

The shell-model transition amplitudes for the 0^+_g to 4^+_1 transition in ^{90}Zr produce a PWBA form factor peaking at 1.0 fm^{-1} with a value of 4.75×10^{-2}. In the valence core-polarization model an $E4$ effective added charge of $0.52e$ is thus required to normalize the experimental and theoretical form-factor maxima. The corresponding transition densities are shown in Fig. 3. Again, the theoretical density with this core-polarization correction is similar in shape to the experimental density, but now the radial position of the model peak falls inside of the experimental peak position to an appreciable extent. Of course this could be cured by use of a different oscillator length than the constant value we are using here. As an alternative we explore the Tassie core-polarization model. The valence density together with same $0.52e$ added effective charge in the Tassie model produces a form factor and a transition density which have smaller maximum values than are found experimentally, even though the $B(E4)$ values of the two composite models are the same. An added charge of $0.85e$ is needed in the Tassie model to bring the theoretical form-factor maximum up to the experimental value. Even so, this value still leaves the cal-

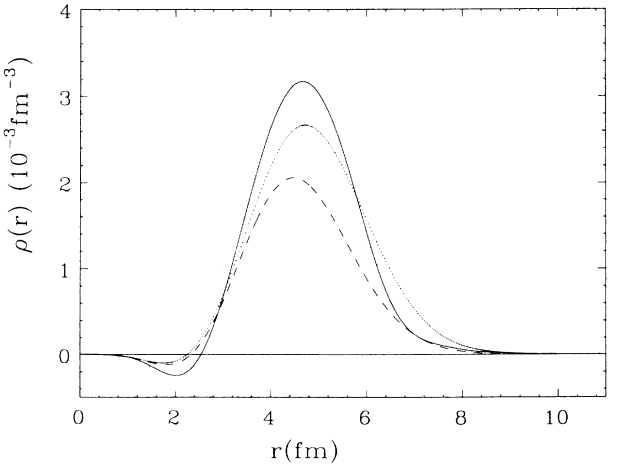

FIG. 3. Charge densities from the first 0^+ to the first 4^+ transition in the ^{90}Zr nucleus. Different curves have the same meaning as in Fig. 1, except the heavy-dotted curve represents the total transition density in the Tassie core-polarization model.

culated density with a smaller peak value than is extracted experimentally. At the same time, the Tassie result greatly exceeds the experimental value in the surface region.

In qualitative terms, both the calculated and the experimentally based densities are characterized by a dominant maximum arising from the $0g_{9/2}^2$ amplitude and a small interior peak of the opposite sign. This interior peak arises in the model from the $0f_{5/2}$-$1p_{1/2}$ amplitude and the correspondence between experiment and theory is related to the relative strengths of this terms in the model and actual wave functions. The negative sign of the interior peak corresponds to constructive interference of the two amplitudes in the surface region.

The 2^+ transition density (see Fig. 4) calculated from the model amplitudes is much smaller than the experimental values in the peak region. In order to normalize the theoretical and experimental form-factor maxima in the valence core-polarization model an added effective charge of $0.96e$ is required. As with the 4^+ data, this normalization produces a density with a maximum well matched to the experimentally derived density but one which has its peak at too small a value of r. The consequences of using a Tassie core-polarization model are also similar to those obtained for the 4^+ transition, but accentuated. In order to match the experimental form-factor maximum a Tassie-model added effective charge of $1.1e$ is required. This leaves a theoretical transition density which has a smaller maximum value than is experimentally extracted and which is significantly larger than the experimental shape near the nuclear surface.

The experimental transition density for the first 2^+ transition shows an appreciable interior peak of the same sign as the dominant $0g_{9/2}^2$ peak. Our model result has an interior peak of the opposite sign, which originates, as in the case of the 4^+ transition, from the $0f_{5/2}$-$1p_{1/2}$ term. In order to obtain a positive (relative to the main) interior peak we would have to have an opposite sign for the $0f_{5/2}$-$1p_{1/2}$ contribution, such that it yielded destructive interference with the $0g_{9/2}^2$ term in the surface region, or, alternatively, have much smaller $0f_{5/2}$-$1p_{1/2}$ amplitudes and much larger $1p_{3/2}$-$1p_{1/2}$ or $1p_{3/2}^2$ amplitudes. If the $1p^2$ amplitudes were to be the source of the positive interior peak they would have to have opposite signs to the very small terms in the presently calculated one-body amplitudes.

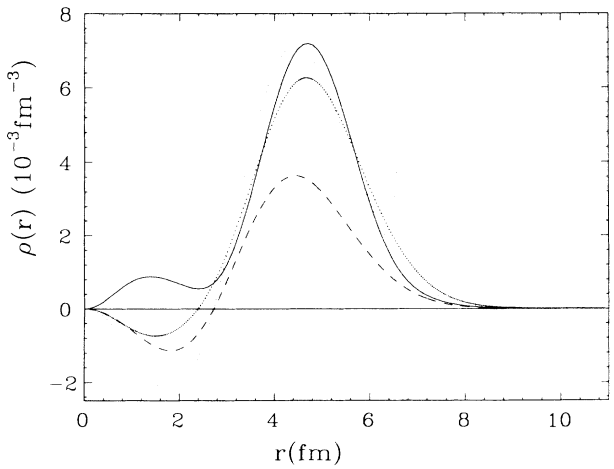

FIG. 4. Charge densities from the first 0^+ to the first 2^+ transition in the ^{90}Zr nucleus. Different curves have the same meaning as in Fig. 3.

VI. CONCLUSIONS

The comparisons we have presented here suggest that our four-orbit $N=50$ shell-model wave functions correctly account for the collective and single-particle features of the lowest-lying states in these nuclei. Most of the matrix elements available for study are dominated by the $0g_{9/2}$ and $1p_{1/2}$ orbits. In particular, many of the magnetic-moment and $B(E2)$ values stem from states which are dominated by $0g_{9/2}^n$ configurations. For these states the variations in magnitude with the number of protons are reproduced quite well with the model wave functions, but these results are not essentially different from those obtained previously with smaller orbit spaces. Simple renormalizations of the $M1$ and $E2$ operators, an enhancement (quenching) of the orbital (spin) part of the $M1$ operator, and a constant added effective charge of $1.0e$ for the $E2$ operator, serve to reproduce the absolute experimental magnitudes. These same renormalizations serve adequately to also reproduce some of the more complex transitions in ^{90}Zr and lighter nuclei, in which mixing between competing $0g_{9/2}$ and $1p_{1/2}$ configurations and the onset of dominance of the $1p_{3/2}$ and $0f_{5/2}$ orbits greatly expands and complicates the simple $0g_{9/2}$ regime. However, the paucity of electromagnetic data below ^{90}Zr precludes definitive conclusions about the less-well-studied $0f_{5/2}$-$1p_{3/2}$ structures. Additional experimental information on the nuclei below ^{90}Zr is essential to fully evaluating the overall success of our model space and Hamiltonian.

The $M4$ isomers in the odd-mass nuclei from $A=89$ to 95 also illustrate the transition from rather pure $0g_{9/2}$ wave functions for the heavier nuclei to transitions in the lighter systems which can only be understood quantitatively with the introduction of configuration mixing across ^{88}Sr as introduced in our model.

Much information[14–16,31] from electron scattering remains to be analyzed. While the $0g_{9/2}^2$ dominated transitions analyzed here are adequately described with conventional effective charge models, data for higher-lying, more complex states might accentuate the discrepancies between our current model results and experiment which are suggested by the deviations in $B(E2)$ values noted in Table II. With the insight into excited-state wave functions provided by these experimental transition densities, it should be possible to correct the data set of level energies which we used in Ref. 1 and thereby to produce an improved Hamiltonian and model wave functions.

ACKNOWLEDGMENTS

We thank Dr. Alex Brown for many useful discussions and the use of his DENS code. This work was supported in part by the National Science Foundation, Grant Nos. PHY87-18772, PHY85-05682, and PHY86-04197.

[1]X. Ji and B. H. Wildenthal, Phys. Rev. C **37**, 1256 (1988).
[2]I. Talmi and I. Unna, Nucl. Phys. **19**, 225 (1960).
[3]S. Cohen, R. D. Lawson, M. H. Macfarlane, and M. Soga, Phys. Lett. **10**, 195 (1964).
[4]N. Auerbach and I. Talmi, Nucl. Phys. **64**, 458 (1965).
[5]J. Vervier, Nucl. Phys. **75**, 17 (1966).
[6]J. B. Ball, J. B. McGrory, and J. S. Larsen, Phys. Lett. **41B**, 581 (1972).
[7]D. H. Gloeckner and F. J. D. Serduke, Nucl. Phys. **A220**, 477 (1973).
[8]J. Blomqvist and L. Rysdtrom, Phys. Scr. **31**, 31 (1985).
[9]T. A. Hughes, in *Proceedings of the International Conference on Properties of Nuclear States, Montreal, 1969,* edited by M. Harvey *et al.* (Presses de l'Université de Montréal, Montréal, Canada, 1969).
[10]C. Dedes and J. M. Irvine, J. Phys. G **1**, 865 (1975).
[11]D. K. Fujita and T. Komoda, Prog. Theor. Phys. **60**, 178 (1978).
[12]H. C. Chiang, M. C. Wang, and C. S. Han, J. Phys. G **6**, 345 (1980).
[13]M. M. Gazzaly *et al.*, Phys. Rev. C **28**, 294 (1983).
[14]J. Heisenberg *et al.*, Phys. Rev. C **29**, 97 (1984).
[15]O. Schwentker *et al.*, Phys. Rev. Lett. **50**, 15 (1983).
[16]O. Schwentker *et al.*, Phys. Lett. **112B**, 40 (1980).
[17]P. J. Brussaard and P. W. M. Glaudemans, *Shell-Model Applications in Nuclear Spectroscopy* (North-Holland, Amsterdam, 1977).
[18]D. Zwart, Comput. Phys. Commun. **38**, 565 (1985).
[19]S. Raman *et al.*, At. Data Nucl. Data Tables **36**, 1 (1987).
[20]*Table of Isotopes,* 7th ed., edited by C. M. Lederer and V. S. Shirley (Wiley, New York, 1978).
[21]P. M. Endt, At. Data Nucl. Data Tables **26**, 47 (1981); **23**, 547 (1979).
[22]B. A. Brown, P. M. S. Lesser, and D. B. Fossan, Phys. Rev. C **13**, 1900 (1976).
[23]W. F. Piel, Jr. *et al.*, Phys. Rev. C **28**, 209 (1983).
[24]A. Amusa and R. D. Lawson, Z. Phys. A **307**, 333 (1982).
[25]J. Bendahan *et al.*, Phys. Rev. C **33**, 1517 (1986).
[26]O. Hausser *et al.*, Nucl. Phys. **A293**, 248 (1977).
[27]I. S. Towner, Phys. Rep. **155**, 263 (1987).
[28]J. Heisenberg and H. P. Blok, Annu. Rev. Nucl. Part. Sci. **33**, 569 (1983).
[29]B. A. Brown, R. Radhi, and B. H. Wildenthal, Phys. Rep. **101**, 314 (1983).
[30]T. E. Milliman *et al.*, Phys. Rev. C **32**, 805 (1985).
[31]L. T. van der Bijl, Ph.D. thesis, Free University of Amsterdam, 1982.